Magneto-Oscillations and Landau Quantization in Decoupled Epitaxial Graphene Multilayers

David L. Miller[1&], Kevin D. Kubista[1&], Gregory M. Rutter[2], Ming Ruan[1], Walt A. de Heer[1], Phillip N. First[1]*, Joseph A. Stroscio[2]*

[1]School of Physics, Georgia Institute of Technology, Atlanta, GA 30332
[2]Center for Nanoscale Science and Technology, NIST, Gaithersburg, MD 20899

& These authors contributed equally to this work
* To whom correspondence should be addressed: first@physics.gatech.edu, joseph.stroscio@nist.gov

Abstract:

The cyclotron motion of electrons in a magnetic field has historically been a powerful probe of the Fermi surface properties of metals and two-dimensional electron systems. Oscillations in many measurable properties such as magnetization, thermal conductivity, and resistance, all reflect the quantization of closed orbits and the resulting discrete density of states. Here we show magneto-oscillations in scanning tunneling spectroscopy of epitaxial graphene as a function of both magnetic field and electron energy. Sharp Landau levels are found in the spectra from the topmost layer of multilayer epitaxial graphene grown on SiC($000\bar{1}$). The spectra are characteristic of 2-dimensional Dirac electron and hole quasiparticles in single-layer graphene. We attribute this to rotational stacking domains that effectively decouple the carbon layers electronically, thereby yielding single-layer graphene properties via a large-area growth method.

A fundamental challenge in the development of new electronics based on a single atomic sheet of carbon, known as graphene, is to realize a large area production method that preserves the intrinsic properties of a single sheet of graphene. To this end, multilayer epitaxial graphene (MEG) grown on SiC substrates has been proposed as a possible platform (*1-3*). A central issue is whether MEG can reproduce the properties of single-layer graphene, with the same intrinsic electronic properties and electrical transport. A number of experiments have shown promising qualities for MEG such as: high carrier mobility (*4*), distinct evidence of chiral charge carriers (*5*), the observation of a Dirac-Weyl linear energy spectrum (*6-8*), and optical transitions between graphene-like Landau levels (LL's) (*9*). Remarkably, these properties persistent to room temperature (*10*). Still, a perceived hallmark of graphene (*11, 12*) is the observed "half-integer" quantum Hall effect (QHE), a manifestation of the Landau-level spectrum of chiral Dirac charge carriers in a magnetic field. To date, this has not been observed in multilayer epitaxial graphene on SiC. Possible explanations for the absence of a QHE in MEG range from the multilayer nature of the material (*13*), to the lack of suitable defects for Anderson localization (*2, 14*).

In this work, we circumvent the technical challenges of gating the multilayer and contacting only a single graphene sheet through non-perturbative methods to measure magneto-oscillations that are analogous to the well-known Shubnikov-de Haas oscillations (SdHO's) of magnetoresistance. Using the scanning tunneling microscope (STM) at low temperature, we detect oscillations in the tunneling differential conductance (*dI/dV)* as a function of an applied external magnetic field; "tunneling magneto-conductance oscillations" (TMCO's). This new method is used to map extended portions of the electronic band structure, in contrast to traditional magnetic oscillations that probe only the Fermi level. Conventional scanning

tunneling spectroscopy (STS) *dI/dV* spectra as a function of tunneling bias V_B have also been acquired at fixed magnetic fields. These spectra show sharp Landau levels for both electron and hole carriers, with line-widths comparable to high mobility semiconductor 2-dimensional electron systems that exhibit the QHE (*15*). Additionally, we use spatial *dI/dV* maps of the zero index Landau level energy (i.e., the Dirac-point energy E_D) to measure local potential variations on the top graphene layer, which are shown to be small over hundreds of nanometers.

The experiments were performed in a custom-built cryogenic ultra-high vacuum STM with high-magnetic-field capability at the National Institute of Standards and Technology (NIST). All experiments were performed at 4.3 K. The MEG sample was grown at the Georgia Institute of Technology on hydrogen-etched carbon-face 4H-SiC($000\bar{1}$) using a low-vacuum induction furnace method (*2*). The graphene thickness was (10 ± 1) layers as determined by ellipsometry measurements. The sample was transported to NIST in air and re-heated to 1250 °C in ultra-high vacuum to remove any contamination. Iridium probe tips prepared by heat treatment and field-evaporation were used for tunneling. TMCO measurements, described below, were performed by sweeping the magnetic field at 0.04 T/min and measuring *dI/dV* with a lock-in amplifier at constant tunneling current and sample bias. *dI/dV* spectra as a function of tunneling bias were recorded in constant magnetic field with the tip-sample distance held fixed and using a root-mean-square modulation voltage of 1 mV superimposed on the sample bias at a frequency of 500 Hz. These two methods are complementary as they each measure a *dI/dV* slice in the 2-dimensional *(B,E)* plane at either fixed *E* (TMCO spectra) or fixed *B* (conventional *dI/dV(E)* spectra).

Figure 1A shows a schematic of the low-energy electronic structure for single-layer graphene. Applying a perpendicular magnetic field causes the electron and hole-states to condense into LL's, indicated by the projected circular cross sections intersecting the conical dispersion. Unlike conventional 2D systems with parabolic dispersion, the LL energies E_n of graphene are not equally spaced: $E_n = \mathrm{sgn}(n)c^*\sqrt{2e\hbar B|n|}$, $n = \ldots -2, -1, 0, 1, 2, \ldots$ (see Fig. 1A) where c^* is the characteristic carrier velocity, e is the elementary charge, and $\hbar$ is Plank's constant divided by 2π. The unique *n=0* LL at $E_0 = E_D$ is not present in a conventional 2D system, and is at the heart of the half-integer QHE. The physics of the *n=0* LL (LL_0) itself is presently under active study theoretically, due to the possibility of novel topological and correlated states, and because of its effect on screening (*16-18*).

Physical measurements of Landau-quantized systems exhibit characteristic oscillations in many properties as the LL's move through the Fermi level E_F with changing magnetic field. Figure 1B shows experimental measurement of tunneling magneto-conductance oscillations in the *dI/dV* signal from multilayer epitaxial graphene as the magnetic field is swept from 0 T to 2.0 T at a tunneling bias of -65 mV (*dI/dV*(*E,* **r**) is proportional to the sample density of states at energy *E* and position **r** (*19*)**)**. These oscillations are similar to SdHO's in conventional magnetoresistance measurements. However, TMCO's are not restricted to E_F but are measured as a function of energy *E*, with $E - E_F = eV_B$ determined by the tunneling bias and where E_F corresponds to V_B=0 (Fig. 1A). As indicated in Fig. 1A, the *dI/dV* signal will oscillate as the density of states due to the LL's move through the energy position $E = eV_B$; a maximum in *dI/dV* occurs at fields where $E_n = eV_B$ (Fig. 1B). For SdHO's, the frequency of oscillations in 1/*B* is

given by, $B_F = (\hbar / 2\pi e)A_F$, with A_F the cross-sectional area of the Fermi surface in a plane normal to the magnetic field (*20-22*). In our measurements, the TMCO frequency B_E is given by the same expression, except that A_F is replaced by A_E, where A_E is the cross-sectional *k*-space area at energy $E = eV_B$ (Fig. 1A). This new method allows the energy dispersion to be measured with very high accuracy in both energy and crystal momentum as *E* is varied via the tunneling bias.

For graphene, we assume circular constant-energy contours of area $A_E = \pi k_E^2$, to determine the graphene wavevector $k_E = (4\pi e / h)B_E^{1/2}$. The inset to Fig. 1B shows a "fan plot" of LL index measured from the TMCO peak maxima versus 1/*B* for different values of tunneling bias V_B. This yields a range of oscillation frequencies B_E corresponding to different constant energy contours A_E (see fig. S1 (*23*)). This is analogous to changing the gate voltage in conventional transport measurements; thus we circumvent the challenge of gating in the MEG system. The fan plot intercepts all fall close to zero indicating a Berry phase of π characteristic of graphene (*24*). Fig. 1C shows the energy-momentum dispersion determined from the TMCO measurements for energies within ± 125 meV of E_D. A fit to the TMCO data determines a characteristic velocity of $c^* = (1.070 \pm 0.007) \times 10^6$ ms^{-1} for both electrons and holes (*25*), with the Dirac point energy 29.2 ± 0.6 meV above the Fermi level (the range of observed E_D values is discussed below). Note that the dispersion measurement in Fig. 1C includes the unfilled electronic states, a regime that is not accessible by photoelectron emission spectroscopy.

The Landau quantization of the density of states that gives rise to the TMCO's can be directly measured in the *dI/dV* spectra at fixed magnetic field. Figure 2A contains over 20 LL's in the tunneling spectrum obtained on MEG in an applied field of 5 T. The LL peaks are extremely sharp compared with similar spectra from semiconductor 2D electron systems or bulk graphite (*26-28*). Evidence for massless Dirac-fermions can be easily inferred by the observation of the LL_0 peak at 7 mV, and the large energy gaps on either side of LL_0 with zero differential conductance. Small features in the spectrum near the $n = 0$ and $n = -1$ LL remain unexplained; these may be due to defect scattering as they vary somewhat with spatial position (see Fig. 3) or they may be intrinsic fine structure of the LL state, particularly for the *n=0* LL, where the 4-fold degeneracy is known to be removed at high magnetic fields (*29*). The LL spectrum in Fig. 2A fits well to a simple sum of Lorentzian lineshapes convolved with a Gaussian instrument function to account for thermal and modulation broadening of fixed 2.8 meV width (*i.e.*, Voigt lineshapes). As shown by the red line in Fig. 2A, the fit accounts for essentially all of the original spectral weight in the density of states, *i.e*. the rising background is dominated by the Lorentzian tails of each LL, which are determined by the carrier lifetimes. To investigate the coupling between graphene layers, we fit the LL energies in Fig. 2A to a bilayer model for different values of the interlayer coupling γ_1 (Fig. 2B inset) (*30*). An interlayer coupling of 300 meV to 400 meV has been measured for Bernal-stacked graphene bilayers (*31, 32*), yet the best fit to the spectrum in Fig. 2A is clearly with zero-interlayer coupling $(\gamma_1 = 0)$.

Figure 2B shows a series of *dI/dV* spectra for different magnetic fields. The LL peaks increase in intensity with increasing energy-separation as the magnetic field is increased. A slight shift of LL_0 is also observed with increasing field. The Dirac point E_D lies below the

Fermi level at low fields (–1.8 meV at 1 T) and shifts to a position of 13.1 meV above E_F at 6 T (Fig. 2C inset). Extrapolating the LL_0 position to zero field yields a Dirac point $E_D = -3.7$ meV at B=0, corresponding to an electron doping of n=8.8 x 10^8 cm^{-2}. This small charge density in the top layer results from the decay in the charge profile through the multilayer stack from the highly doped interface layer (*33*), and is similar to that seen in optical measurements (*9, 10*). The shift of the Dirac point with field results from the redistribution of charge in the multilayer determined by the degeneracy of the available LL's, and the effective screening perpendicular to the graphene planes (*33*). The shift of LL_0 across the Fermi level is not completely understood at present, and could be influenced by the electrostatic potential derived from the difference in the probe tip and graphene work functions. More detailed theoretical analysis on the screening properties of the Dirac carriers in the presence of a tip potential and a constant magnetic field is required for a complete understanding of these results.

Further confirmation of single layer electronic structure comes from the scaling of LL energies E_n with magnetic field at high fields. For the Dirac spectrum, E_n should scale as $\sqrt{B}$ (see above) whereas in all other forms, including bilayer graphene and graphite, the LL's scale linearly in B for energies near the Dirac point. Remarkably, a complete linear collapse of all the LL's energies is obtained by plotting E_n versus $\sqrt{|n|B}$ (Fig. 2C). The degree of linearity of the LL dispersion in Fig. 2C is high, confirming Dirac quasiparticles in this MEG system. Fitting both electron and hole branches in Fig. 2C yields a carrier velocity of $c^* = (1.128 \pm 0.004)$ x 10^6 ms^{-1} in good agreement with the range of values reported for graphene (*34*). Close inspection of Fig. 2C shows that the electron and hole states actually have

slightly different velocities. Independent fits to the two branches give velocities $c^* = (1.189 \pm 0.007)$ x 10^6 ms^{-1} for the states below E_D and $c^* = (1.044 \pm 0.004)$ x 10^6 ms^{-1} for states above E_D. The 6 % difference observed between these values may imply a breakdown of electron-hole symmetry. A similar asymmetry, although two times smaller, was recently observed in cyclotron resonance studies of exfoliated graphene (*34*). However, some contribution to the electron-hole asymmetry observed in Fig. 2C could also be due to the screening of the tip electric field (band bending), requiring a small correction to the energy scale in Fig. 2C. Calculations of the multilayer screening by the Dirac carriers in the presence of a tip potential and a constant magnetic field indicate such corrections are present to a small degree (*33*).

Spatial variation of the Landau level energies, particularly the LL_0, can be used to map fluctuations of the local potential. Figures 3A and B show a topographic image and corresponding spatial map of the LL_n energies (vertical) and *dI/dV* intensities (color scale) for (n=0,-1,-2,-3) along the line marked in Fig. 3A. The average position of E_D is 55.2 meV above E_F, with a variance of ± 1.9 meV (Fig. 3C). By far, the largest variation corresponds to a subsurface rotational domain boundary that occurs in the center of the image (the top graphene layer is atomically continuous over the boundary). These variations in LL position show an extremely smooth potential variation (and hence carrier density), in contrast to the electron and hole puddles observed for exfoliated graphene on SiO_2 substrates (*35*). In surveying the sample, a variation of approximately ± 25 meV in the E_D was observed over distances of many tens of microns (see E_D differences between Figs. 2 and 3), still considerably smaller than the variations seen in exfoliated systems on SiO_2. The large density fluctuations on SiO_2 substrates apparently

result from charged impurities in the SiO_2. The smooth charge/potential contour of MEG could be due to screening of the interface potential fluctuations by the graphene multilayer, and the crystalline SiC substrate may be more homogenous than the amorphous SiO_2 substrate with respect to trapped charges.

The *dI/dV* spectra in Fig. 2 agree very well with the LL spectrum expected for massless Dirac fermions, implying that the topmost layer of MEG closely approximates an isolated sheet of graphene. We attribute this to electronic decoupling of the graphene layers in MEG grown on the carbon-face of SiC as a consequence of rotational stacking faults between layers (*36*). A variety of rotational stacking angles are found in STM topographic images of the surface of MEG (fig. S2) (*23*). Slight rotations of one layer with respect to the next create moiré super-periods superimposed on the atomic lattice (fig. S2) (*23, 36*). The ≈0.02 nm peak-to-peak height modulation originates from periodically-varying alignment of top-layer atoms with those below, but the exact source of image contrast is still a subject of debate (*37*). Our survey of the carbon-face grown sample showed moiré patterns of various periods in almost every location examined with spectra similar to those seen in Fig. 2.

In addition to the spatial homogeneity of the LL spectra, we observe that the linewidths of the Landau levels are very small. In particular we measure a Lorenztian linewidth of 1.5 meV for LL_0 in Fig. 2A, after accounting for instrumental broadening (2.8 meV Gaussian). Associating this width with a characteristic scattering time, $\tau = \hbar / \Delta E$, yields $\tau = 0.4$ ps; the momentum relaxation time, which determines the transport mobility, will be substantially larger (*38*). We note that these samples are relatively low in defects; the STM topographs indicate a

density of ≈ 1 point defect per 100 nm x 100 nm area on the top layer. It is interesting to discuss the sharp Landau quantization observed here with the *lack* of the QHE in transport measurements in this MEG system. The QHE is similarly absent in suspended exfoliated graphene samples that exhibit very high mobility and low defect density (*39*). Prior speculation and recent theoretical examinations of the QHE in graphene point out the necessity of disorder-induced Anderson localization for the observation of the QHE (*2, 14*). Our observation of sharp Landau levels, with apparently vanishingly small density of localized states, is consistent with the absence of the integer QHE in epitaxial graphene.

In summary, we have measured 1/B oscillations in the tunneling differential conductance of multilayer epitaxial graphene from a scanning tunneling microscope probe. This demonstrates that the local STM probe determines the extended electronic structure of this low-density system. We have shown the existence of sharp Landau levels in multilayer epitaxial graphene, with energy and magnetic field dispersion accurately modeled by the electronic structure of an isolated graphene sheet. Spectroscopic maps over hundreds of nanometers show minimal potential fluctuations in the graphene sheets. These single layer graphene characteristics may be useful for carbon electronics based on multilayer epitaxial graphene, which could be easily grown over large wafers of silicon carbide.

Acknowledgements: We thank Allan MacDonald, Hongki Min, Mark Stiles and the NIST graphene team for valuable comments and discussions. We also thank Claire Berger, Nikhil Sharma, Mike Sprinkle, Steven Blankenship, Alan Band, and Frank Hess for their technical

contributions to this work. Portions of this work were supported by NSF (ECCS-0804908), by the NRI-INDEX program, and by the W. M. Keck Foundation. Graphene production facilities were developed under NSF grant ECCS-0521041.

Reference List

1. C. Berger *et al.*, *Journal of Physical Chemistry B* **108**, 19912 (2004).
2. W. A. de Heer *et al.*, *Solid State Communications* **143**, 92 (2007).
3. A. K. Geim, K. S. Novoselov, *Nature Materials* **6**, 183 (2007).
4. C. Berger *et al.*, *Science* **312**, 1191 (2006).
5. X. Wu, X. Li, Z. Song, C. Berger, W. A. de Heer, *Physical Review Letters* **98**, 136801 (2007).
6. E. Rolling *et al.*, *Journal of Physics and Chemistry of Solids* **67**, 2172 (2006).
7. T. Ohta *et al.*, *Physical Review Letters* **98**, (2007).
8. G. M. Rutter *et al.*, *Science* **317**, 219 (2007).
9. M. L. Sadowski, G. Martinez, M. Potemski, C. Berger, W. A. de Heer, *Physical Review Letters* **97**, (2006).
10. M. Orlita *et al.*, *arXiv:0808. 3662v4* (2008).
11. K. S. Novoselov *et al.*, *Nature* **438**, 197 (2005).
12. Y. B. Zhang, Y. W. Tan, H. L. Stormer, P. Kim, *Nature* **438**, 201 (2005).
13. P. Darancet, N. Wipf, C. Berger, W. A. de Heer, D. Mayou, *Physical Review Letters* **101**, (2008).
14. P. M. Ostrovsky, I. V. Gornyi, A. D. Mirlin, *Physical Review B* **77**, (2008).

15. A. Potts *et al.*, *Journal of Physics-Condensed Matter* **8**, 5189 (1996).

16. C. Toke, P. E. Lammert, V. H. Crespi, J. K. Jain, *Physical Review B* **74**, (2006).

17. Barlas Y., T. Pereg-Barnea, M. Polini, R. Asgari, A. H. MacDonald, *arXiv:cond-mat/0702406* (2007).

18. M. Arikawa, Y. Hatsugai, H. Aoki, *Physical Review B* **78**, 205401 (2008).

19. J. A. Stroscio, W. Kaiser, *Scanning Tunneling Microscopy* (Academic Press Inc., 1993).

20. N. Ashcroft, N. Mermin, *Solid State Physics* (Brooks Cole, London, 1976).

21. V. P. Gusynin, S. G. Sharapov, *Physical Review B* **71**, (2005).

22. S. G. Sharapov, V. P. Gusynin, H. Beck, *Physical Review B* **69**, (2004).

23. Additonal text and data is available online.

24. I. A. Luk'yanchuk, Y. Kopelevich, *Physical Review Letters* **93**, (2004).

25. All uncertainties reported represent one standard deviation in the measured quantity.

26. M. Morgenstern, J. Klijn, C. Meyer, R. Wiesendanger, *Physical Review Letters* **90**, (2003).

27. T. Matsui *et al.*, *Physical Review Letters* **94**, (2005).

28. G. Li, E. Y. Andrei, *Nature Physics* **3**, 623 (2007).

29. Y. Zhang *et al.*, *Physical Review Letters* **96**, (2006).

30. E. A. Henriksen *et al.*, *Physical Review Letters* **100**, (2008).

31. G. M. Rutter, J. N. Crain, N. P. Guisinger, P. N. First, J. A. Stroscio, *Journal of Vacuum Science & Technology A* **26**, 938 (2008).

32. J. Yan, E. A. Henriksen, P. Kim, A. Pinczuk, *Physical Review Letters* **101**, (2008).

33. Hongki Min, Mark Stiles, and Allan MacDonald, private communication.

34. R. S. Deacon, K. C. Chuang, R. J. Nicholas, K. S. Novoselov, A. K. Geim, *Physical Review B* **76**, (2007).

35. J. Martin *et al.*, *Nature Physics* **4**, 144 (2008).

36. J. Hass *et al.*, *Physical Review Letters* **100**, 125504 (2008).

37. W. T. Pong, C. Durkan, *Journal of Physics D-Applied Physics* **38**, R329 (2005).

38. J. H. Davies, *The Physics of Low-dimensional Semiconductors:An Introduction* (Cambridge University Press, Cabridge, United Kingdom, 1998).

39. K. I. Bolotin *et al.*, *Solid State Communications* **146**, 351 (2008).

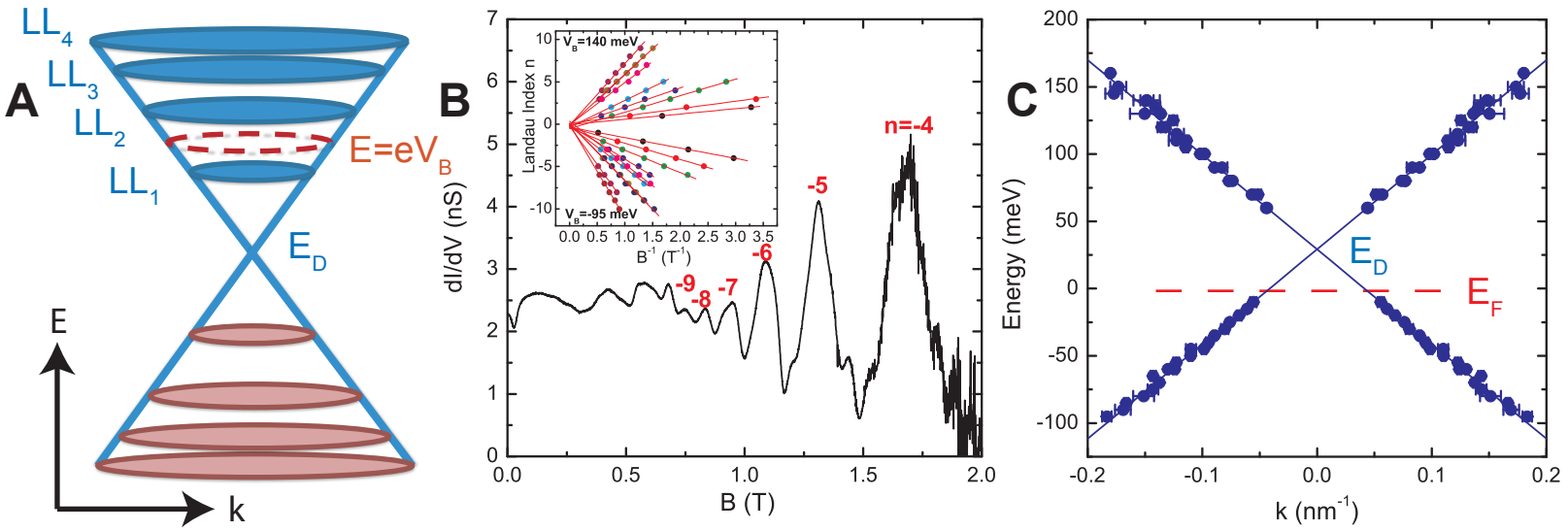

Figure 1: Tunneling magneto-conductance oscillations in epitaxial graphene. (A) Schematic of graphene low energy dispersion with quantized Landau levels (LL_n) in a magnetic field. The Dirac point E_D locates the common apex of the electron and hole cones. The red dashed line indicates the k-space area A_E corresponding to a *dI/dV* measurement at the setpoint energy $E=eV_B$. (B) TMCO's in *dI/dV*(E=-65 meV) as the magnetic field is swept perpendicular to the graphene plane. The largest oscillations originate from the Landau levels sweeping through the energy E. The inset fan plot shows a linear relation in the LL index n from the conductance oscillations vs. $1/B$, yielding the TMCO frequencies B_E. The error in the peak positions is smaller than the symbol size. Each line corresponds to a separate TMCO measurement at different tunneling biases from -95 mV to 140 mV (see fig. S1 (23)). (C) The energy-momentum dispersion (symmetrized about k=0) obtained from the TMCO frequencies B_E. A linear fit yields a carrier velocity $c^*=(1.070 \pm 0.007) \times 10^6$ ms^{-1} and a Dirac point location of $E_D=29.2 \pm 0.6$ meV above E_F (25).

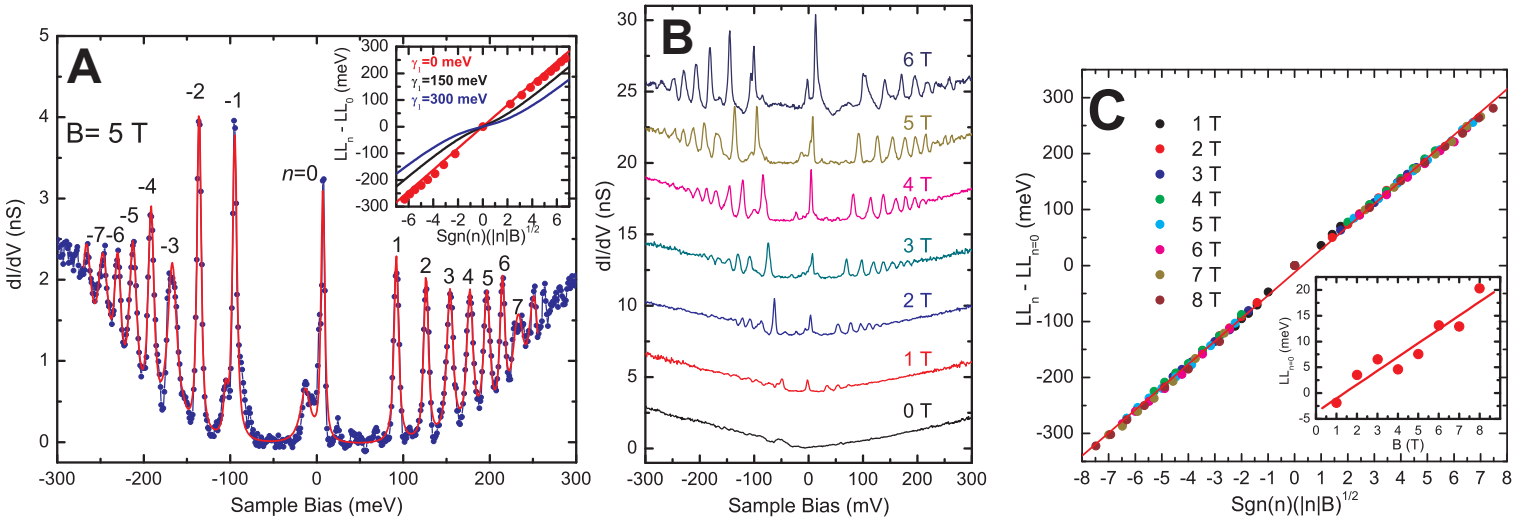

Figure 2: Direct measurement of Landau quantization in epitaxial graphene (A) Blue data points show the tunneling differential conductance spectra vs. sample bias of Landau levels in multilayer graphene at B=5 T. Landau level indices are marked. The red line shows a fit to a series of Voigt lineshapes at the Landau level peak positions, which accounts for essentially all the density of states in the spectrum, (tunneling setpoint, V_B = 350 mV, I= 100 pA). (Inset) LL peak position vs. square root of LL index and applied field from the peak positions in (A). Errors in peak positions are smaller than the symbol size. Solid lines are fits to a bilayer model with interlayer coupling of (red) zero, (black) 150 meV, and (blue) 300 meV. (B) Landau level spectra for various applied magnetic fields from 0 T to 6 T. The curves are offset for clarity, (tunneling setpoint, V_B = 350 mV, I= 100 pA). (C) Landau level peak energies for applied fields of 1 T to 8 T, showing a collapse of the data when plotted versus square root of LL index and applied field. The solid line shows a linear fit yielding a characteristic velocity of c^*=(1.128 ± 0.004) x 10^6 ms^{-1} (25). The inset shows the shift in the LL_0 peak posistion as a function of applied field (symbols). The error is smaller than the symbol size. The solid line is a linear fit to the data points.

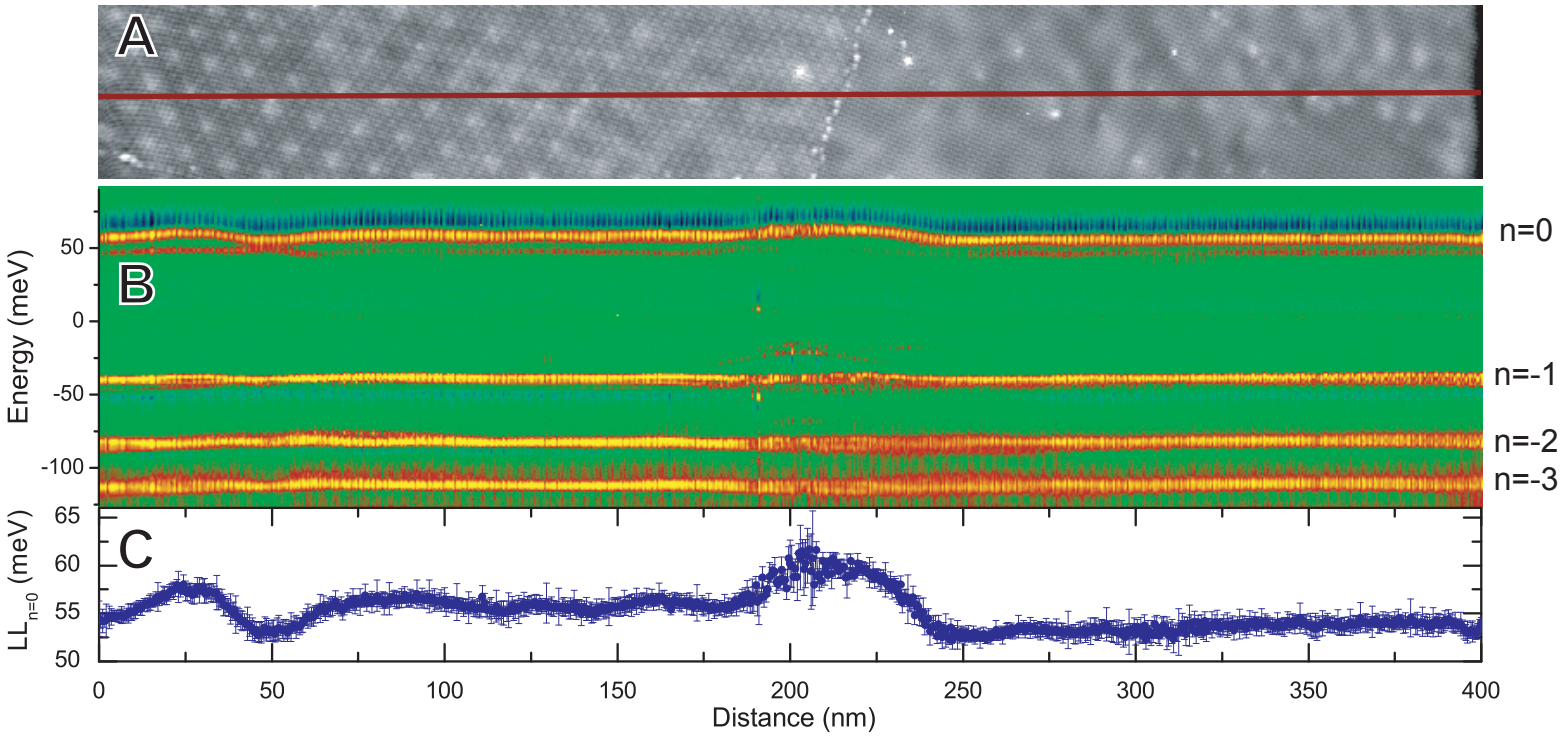

Figure 3: Spatial variation of the surface potential in epitaxial graphene. (A) STM topograph, 50 nm x 400 nm, showing a region containing a boundary between two different moiré regions. Grayscale range 0.3 nm. The periodic features correspond to the moiré (see fig. S2 (23)). (B) A series of *dI/dV* spectra obtained along the center horizontal line in (A) showing low-lying Landau levels. Image color is the *dI/dV* intensity (blue -1.5 nS to yellow 2.5 nS), the horizontal axis is distance, and the vertical axis is energy. The Landau level indices are labeled to the right of the image. (C) Variation in the LL_0 peak position as a function of distance along the line indicated in (A). Error bars are one-sigma error in fitting LL_0 peak positions in (B).

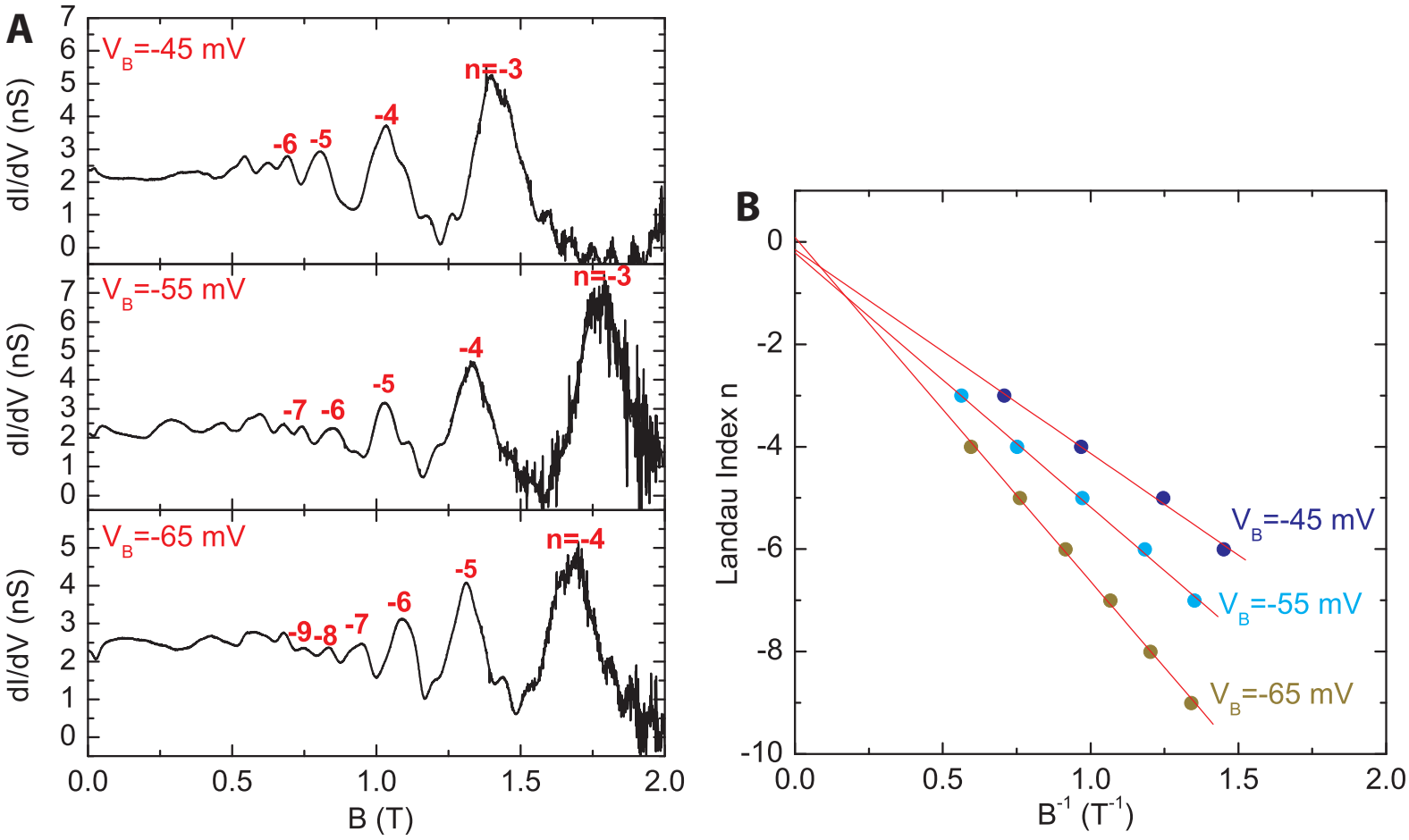

Figure S1: (A) Tunneling magneto-conductance oscillations as a function of tunneling bias V_B. Landau level indices are indicated above the peaks. (B) Landau level index n versus $1/B$ for the three TMCO spectra in (A). A linear fit to the Landau level index n vs $1/B$ data yields the oscillation frequencies B_E used to determine the energy-momentum dispersion relation in Fig. 1C. B_E= -3.2, -5.3, and -6.8 T for V_B=-45, -55, and -65 mV. A larger collection of similar data is shown in the inset to Fig. 1B.

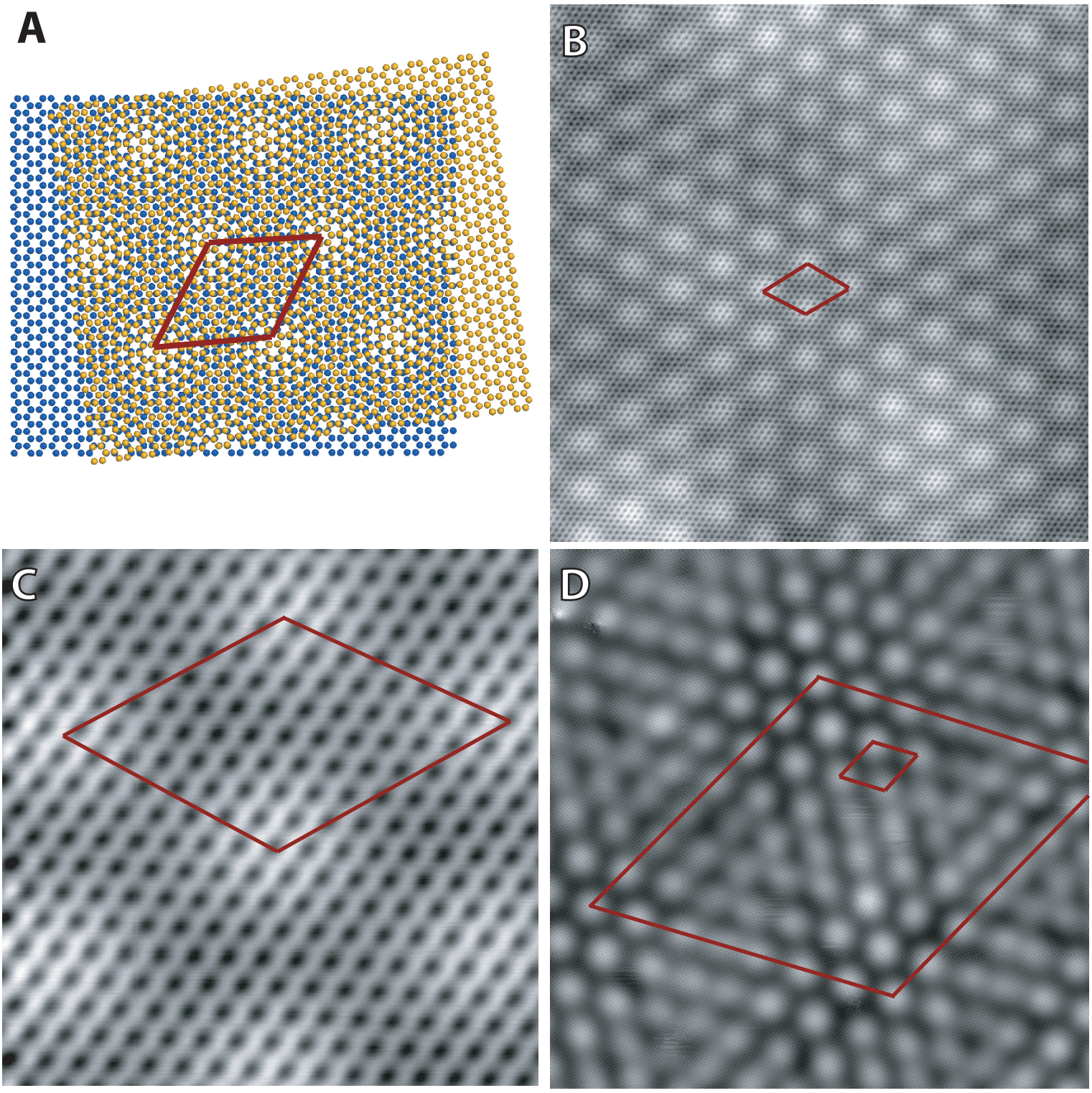

Figure S2: Moiré patterns from rotational stacking of graphene layers. (A) Schematic drawing illustrating the rotation of two hexagonal lattices by a small angle (7 degrees) which gives rise to a super-periodicity with a large unit cell, shown in red. (B) STM topographic image, 20 nm x 20 nm, showing a moiré pattern with a unit cell length of 1.9 nm corresponding to a rotation angle of 7.42 degrees. (C) Zoomed region from the area in (B), 3.8 nm x 3.8 nm, showing the graphene hexagonal lattice within the moiré pattern. (D) STM topographic image, 47 nm x 47 nm, showing a double moiré pattern with a small and large unit cell. The unit cells correspond to rotations between two layers of 0.47 degrees, and two other layers of 4.13 degrees.